Science Advances
AAAS

Supplementary Materials for

Self-supervised AI for decoding and designing disordered metamaterials

Min Shen *et al.*

Corresponding author: Ke Liu, liuke@pku.edu.cn; Sheng Mao, maosheng@pku.edu.cn

Sci. Adv. **12**, eadx7389 (2026)
DOI: 10.1126/sciadv.adx7389

The PDF file includes:

Supplementary Text
Table S1
Figs. S1 to S11
Legends for movies S1 and S2
References

Other Supplementary Material for this manuscript includes the following:

Movies S1 and S2

Detailed Architecture of Generator and Discriminator

A diagram of the structure of the discriminator and generator of the three-parameter case is presented in Fig. S1. The orange arrows denote the downsampling direction, executed by the convolution neural network (CNN), and the blue arrows indicate the upsampling direction, executed by the transposed convolution neural network.

We adopt a structure similar to deep convolutional generative adversarial networks (DCGAN)[50] for our discriminator. Here, we replace batch normalization with instance normalization. This change is due to the impact of batch normalization that alters the problem formulation for the discriminator. Changes the mapping from a single input to a single output to that of an entire batch of inputs to a batch of outputs[51], which makes the penalized training objective no longer valid in this network architecture. The embedding network consists of three fully connected layers with 16 channels, using conditional batch normalization[52] for convolutional feature maps.

We use three latent codes, c_1, c_2, c_3, to extract different types of geometric features related to the target properties. The first two latent codes, c_1 and c_2, are mapped to the embeddings by the embedding networks. Then these embeddings are injected into the 1×1 and 16×16 feature layers with conditional batch normalization mechanism, respectively.The size of the receptive field for c_1 is 64×64, which helps capture the global injection information, while for c_2, the size of the receptive field whose size is 19×19, extracts the local information. As for c_3, its main objective is to capture periodic features such as orientations of anisotropy. For this reason, we take the sine and cosine values of c_3 and then inject the values into the generator's 8×8 layer.

Note that we take scale-free input noise templates and latent codes as the input for the generator. To control the local microstructure, the input mechanism of the local latent codes should align each local input noise template using the conditional batch normalization mechanism. This method allows for the design of functionally graded materials, as illustrated in Fig. S8 S9 S10, and the flexible modification of the local multi-physical properties.

Fabrication and measurement

To further validate the prediction of our approach, we first fabricated the designed materials and then measured their mechanical properties. To do so, we first generate material images using the GNDM. We selected 10 parameter sets for validation S1. We binarize the output image, in which the binary matrix (1-0) represents the soft and hard phases, with "1" indicating the hard phase and "0" indicating the soft phase. To prepare the testing samples, we generated material images, which were subsequently converted into 3D test samples by extending them to a thickness of 10 pixels using 3D modeling software.

Each specimen had a 16 mm-long, 16 mm-wide gauge section with a uniform thickness of 2 mm, transitioning through smooth fillets to 24 mm-wide, 4 mm-thick grip ends; the overall end-to-end length was 66.4 mm. The transverse directions, axial (loading) and thickness are designated x, y and z, respectively, to preserve a consistent frame of reference for both experiments and finite-element modeling.

Dog-bone-shaped tensile coupons were additively manufactured on a Stratasys® Objet500 Connex3™ multimaterial PolyJet® 3D printer (materialjetting technology). A dualmaterial build strategy was employed to represent a compliant/rigid composite: the soft phase was printed with AGILUS photopolymer, while the rigid phase was printed with VeroPureWhite photopolymer.

To probe the directional elastic response, two principal print orientations were defined relative to the printers Xscan direction to characterise the builddirection anisotropy of the additively manufactured material. In the *longitudinal (L)* configuration, the coupons gauge axis was aligned with the printers Xscan, i.e., the principal raster direction. In the *transverse (T)* configuration, the coupon was rotated 90° about the build (z) axis so that its gauge axis lay perpendicular to the raster direction.

Mechanical testing was conducted on a Mark10 motorised universal test stand (model ESM750) outfitted with interchangeable Mark10 Series load cells rated at 50 N and 1 kN. A constant crosshead displacement rate of $2\,\mathrm{mm}\cdot\mathrm{min}^{-1}$ was applied. Eight highcontrast markers were bonded to the front face of every specimen before testing. One marker was placed at each corner of the gauge section (upperleft, upperright, lowerleft, lowerright), and the remaining four were positioned at the midpoints of the corresponding edges. The experimental process in the tensile test was recorded by a fixed video camera, capturing the entire deformation process at one frame per second.

To compute the stiffness matrix, we first applied an imageprocessing algorithm (OpenCV[53]) to track the temporal positions of the fiducial markers AH on each specimen, as shown in Fig. S3, obtaining their coordinates $[x_i(t), y_i(t)]$ in every frame. The longitudinal strain ε_y was calculated from the change in vertical gauge lengths using

$$\varepsilon_y(t) = \frac{L_y(t) - L_{y0}}{L_{y0}}, \tag{10}$$

where L_{y0} is the initial longitudinal length. Specifically, the vertical distances AD, BE, and CF were used to compute three longitudinal strains, while GH was used to compute the transverse strains.

The tensile force $F(t)$ was recorded simultaneously by the testing machine, and the stress was obtained as

$$\sigma(t) = \frac{F(t)}{A}, \tag{11}$$

where A is the crosssectional area of the specimen. Stressstrain curves were then constructed using the longitudinal strains and the corresponding stresses. To compute the stiffness matrix $\mathbf{E}$, we define it as

$$\mathbf{E} = \begin{bmatrix} E_{11} & E_{12} \\ E_{21} & E_{22} \end{bmatrix}. \tag{12}$$

Each component is obtained from the experimental stressstrain data as follows: From the longitudinal (L) specimens, the average of AD, BE, and CF yields E_{11}, while GH yields E_{12}. Similarly, from the transverse (T) specimens, repeating the same procedure provides E_{22} and E_{21}. Finally, eigenvalue analysis of the stiffness matrix allowed the determination of the maximum Youngs modulus and the anisotropy angle. The tensile force $F(t)$ was recorded simultaneously by the testing machine, and the stress was obtained as

$$\sigma(t) = \frac{F(t)}{A}, \tag{13}$$

where A is the cross-sectional area of the specimen. Stressstrain curves were then constructed using the measured strains and the corresponding stresses. Each component was obtained from the *tangent modulus extracted from fitted stressstrain data. Let ε_L and ε_T denote the longitudinal and transverse strains, and σ_L and σ_T the corresponding stresses for specimens loaded along the longitudinal (L) and transverse (T) directions. In the small-strain regime we approximate the response locally as*

$$\begin{bmatrix} \sigma_L \\ \sigma_T \end{bmatrix} = \begin{bmatrix} E_{11} & E_{12} \\ E_{21} & E_{22} \end{bmatrix} \begin{bmatrix} \varepsilon_L \\ \varepsilon_T \end{bmatrix}, \quad \textit{so that} \quad E_{ij} = \left.\frac{\partial \sigma_i}{\partial \varepsilon_j}\right|_{\varepsilon \to 0}.$$

For each specimen orientation (L and T), the $\sigma\varepsilon$ curves were fitted (least squares) over a small initial strain window, and the derivatives of the fits at the reference strain provided E_{11} and E_{12} from the L tests and E_{22} and E_{21} from the T tests. Finally, eigenvalue analysis of $\mathbf{E}$ was used to determine the maximum Youngs modulus and the anisotropy angle θ.

Fitting the phenomenological formula

We use second-order polynomials as the phenomenological formula in single-parameter cases. To be specific, in the case of single-parameter, the phenomenological formula of code c_1 adopts the following form:

$$\bar{E} = a_1 c_1 + a_2 c_1^2 + a_3, \tag{14}$$

where $\bar{E}$ is the relative Young's modulus, the ratio of the effective Young's modulus of the composite over that of the hard material, and a_1, a_2, a_3 are three non-dimensional coefficients to be fitted. After the process of self-learning, we obtained that $a_1 = 0.177$, $a_2 = 0.022$ and $a_3 = 0.128$.

In the case of three-parameter, three latent codes (c_1, c_2, c_3) are used to fit the probability parameters of target material properties. x_1, x_2, x_3 represent the relative maximum Young's modulus and the relative orientation of the principal modulus, respectively. We use second-order polynomials to fit c_1, c_2 with x_1, x_2, and trigonometric function to fit c_3 in the phenomenological formula. The phenomenological formula is expressed as follows:

$$\begin{bmatrix} x_1 \\ x_2 \\ \arcsin(x_3) \end{bmatrix} = \begin{bmatrix} a_{11} & a_{12} & a_{13} & a_{14} & 0 \\ a_{21} & a_{22} & a_{23} & a_{24} & 0 \\ 0 & 0 & 0 & 0 & a_{35} \end{bmatrix} \begin{bmatrix} c_1 \\ c_1^2 \\ c_2 \\ c_2^2 \\ c_3 \end{bmatrix} + \begin{bmatrix} b_1 \\ b_2 \\ b_3 \end{bmatrix} \tag{15}$$

where $a'_{ij}s$ and $b'_i s$ are the non-dimensional coefficients to be fitted. The use of sine functions are to take into account the fact that orientation is a periodic variable.

The input and output mechanism of the generator for the latent codes is illustrated in Figure S1. The first two latent codes, c_1 and c_2, are input and output from the 1×1 and 16×16 feature layers, respectively. We process the latent code c_3 using trigonometric functions, and its sine and cosine function values are introduced into the generator in the 8×8 layer. By learning the relationship between geometric features and properties, we obtained the following result. The results are shown in Fig. 4:

$$\begin{bmatrix} x_1 \\ x_2 \\ \arcsin(x_3) \end{bmatrix} = \begin{bmatrix} 0.1059 & 0.1598 & -0.070 & 0.0488 & 0 \\ 0.0193 & -0.017 & 0.1069 & 0.0420 & 0 \\ 0 & 0 & 0 & 0 & -0.6731 \end{bmatrix} \begin{bmatrix} c_1 \\ c_1^2 \\ c_2 \\ c_2^2 \\ c_3 \end{bmatrix} + \begin{bmatrix} -0.0005 \\ 0.1711 \\ 1.1491 \end{bmatrix} \tag{16}$$

Training time, computational resources

In our current implementation, a single training run takes approximately 43,000 seconds. The training was conducted on a personal workstation equipped with an Intel® Xeon® W–1270P CPU and a Quadro RTX 5000 GPU, with 2 *GB* of GPU memory utilized. The inference time for generating 500 material samples is approximately $0.0196s$ for 64×64 samples, $0.0275s$ for 128×128 samples, and $0.0416s$ for 256×256 samples. Regarding training time, the majority of the computational cost arises from evaluating the maximum stiffness and anisotropy directions via FEM simulations, rather than from neural network training or specific surface area calculations. As the system size increases, the primary bottleneck is the FEM computation, and the overall runtime scales proportionally with the FEM simulation cost. This bottleneck could potentially be mitigated in future work by employing parallel FEM solvers. We also note that if the focus shifts to other material properties, the computational profile may change accordingly. Properties with higher computational complexity will dominate the total runtime, whereas properties that are easier to compute will result in training times that are less sensitive to system size. Regarding computational resources, GPU usage is primarily driven by the convolutional neural network used to process the material images. As the system resolution increases, deeper networks with more parameters are required, leading to GPU memory consumption that approximately grows quadratically with the material size due to the stacking of multiple convolutional layers. This memory usage can be controlled by adjusting the batch size during training. CPU usage is dominated by FEM computations and scales with the computational cost of the corresponding finite element analyses.

Calculation of effective elastic tensor

We follow the classical treatment of asymptotic homogenization to calculate the effective elastic tensor of heterogeneous materials[54]. We start with a strong form of the boundary value problem on a composite domain given as:

$$\sigma^{\zeta}_{ij,j} + b^{\zeta}_i = 0 \qquad \text{on } \Omega^{\zeta} \tag{17a}$$
$$\sigma^{\zeta}_{ij} = L^{\zeta}_{ijkl}\varepsilon^{\zeta}_{kl} \qquad \text{on } \Omega^{\zeta} \tag{17b}$$
$$\varepsilon^{\zeta}_{ij} = u^{\zeta}_{(i,j)} = \frac{1}{2}\left(u^{\zeta}_{i,j} + u^{\zeta}_{j,i}\right) \qquad \text{on } \Omega^{\zeta} \tag{17c}$$
$$\sigma^{\zeta}_{ij} n^{\zeta}_j = \bar{t}^{\zeta}_i \qquad \text{on } \partial\Omega^{t\zeta} \tag{17d}$$
$$u^{\zeta}_i = \bar{u}^{\zeta}_i \qquad \text{on } \partial\Omega^{u\zeta} \tag{17e}$$
$$\partial\Omega^{t\zeta} \cup \partial\Omega^{u\zeta} = \partial\Omega^{\zeta} \text{ and } \partial\Omega^{t\zeta} \cap \partial\Omega^{u\zeta} = 0 \tag{17f}$$

The fourth-order tensor $\mathbb{L}$ denoted as the constitutive tensor satisfying conditions of symmetry and positivity, represents the stiffness coefficients for linear elasticity. For heterogeneous materials, the material coefficients depend on the coordinates. In this case, the governing equations can be expressed as follows:

$$(L_{ijkl}u_{k,l})_{,j} + b_i = 0, \tag{18}$$

where vector b represents the body force, and vector u represents the displacement. Two coordinate vectors are defined: x as the coarse-scale position vector; and y as the fine-scale position vector. These two coordinates are related by $y = x/\zeta$ with $0 < \zeta \ll 1$. Consider the following displacement field ansatz:

$$u_i(x) = u_i^{(0)}(x,y) + \zeta u_i^{(1)}(x,y) + \zeta^2 u_i^{(2)}(x,y) + O(\zeta^3) \tag{19}$$

and plug that into the equilibrium equation 17a, we have the following:

$$\zeta^{-2}\sigma^{(-1)}_{ij,y_j} + \zeta^{-1}\left(\sigma^{(-1)}_{ij,x_j} + \sigma^{(0)}_{ij,y_j}\right) + \left(\sigma^{(0)}_{ij,x_j} + \sigma^{(1)}_{ij,y_j} + b_i\right) + O(\zeta) = 0. \tag{20}$$

For the above equation to hold, we need:

$$\begin{aligned} O\left(\zeta^{-2}\right): &\quad \sigma_{ij,y_j}^{(-1)} = 0 \\ O\left(\zeta^{-1}\right): &\quad \sigma_{ij,x_j}^{(-1)} + \sigma_{ij,y_j}^{(0)} = 0 \\ O(1): &\quad \sigma_{ij,x_j}^{(0)} + \sigma_{ij,y_j}^{(1)} + b_i = 0 \end{aligned} \tag{21}$$

By integrating over a single cell region on both sides of the equation of $O(\zeta^{-2})$, employing integration by parts, utilizing periodic boundary conditions, and considering the positive definiteness of $\mathbb{L}$, the simplified equilibrium formula of $O(\zeta^{-1})$ is obtained:

$$\sigma_{ij,y_j}^{(0)}(x,y) = \left[L_{ijkl}(y)\left(u_{(k,x_l)}^{(0)}(x) + u_{(k,y_l)}^{(1)}(x,y)\right)\right]_{,y_j} = 0 \tag{22}$$

By employing a separation of variables approach to solve the equation and introducing a control equation, we derive:

$$u_k^{(1)}(x,y) = H_k^{mn}(y) u_{(m,x_n)}^{(0)}(x) \tag{23}$$

Utilizing the periodic boundary conditions of the microstructure, numerical solutions can be obtained.

$$\left[L_{ijkl}(y)\left(I_{klmn} + H_{(k,y_l)}^{mn}(y)\right)\right]_{,y_j} = 0 \tag{24}$$

where:

$$I_{klmn} = \frac{1}{2}\left(\delta_{km}\delta_{ln} + \delta_{kn}\delta_{lm}\right) \tag{25}$$

where δ_{km} represents the Kronecker delta. We find $H_i^{mn}(y)$ on Θ of unit cell problem :

$$\left[L_{ijkl}\left(H_{(k,y_l)}^{mn} + I_{klmn}\right)\right]_{,y_j} = 0 \text{ on } \Theta \tag{26a}$$

$$H_i^{mn}(y) = H_i^{mn}(y+l) \text{ on } \partial\Theta \tag{26b}$$

$$H_i^{mn}(y) = 0 \text{ on } \partial\Theta^{\text{vert}} \tag{26c}$$

and l is a period. With homogenization theory, the effective elastic tensor can ultimately be expressed as:

$$E_{kl}^{mn}(y) = I_{klmn} + H_{(k,y_l)}^{mn}(y) \tag{27}$$

The calculation of the maximum Young's modulus and corresponding orientation

Here, we briefly describe how to calculate the maximum Young's modulus and its orientation. According to Hooke's law, the stress-strain relationship of the material can be expressed as:

$$\sigma_{ij} = L_{ijk\ell}\varepsilon_{k\ell} \ (i,j=1,2), \tag{28}$$

or reversely by:

$$\varepsilon_{ij} = S_{ijk\ell}\sigma_{k\ell} \ (i,j=1,2) \tag{29}$$

where $\mathbb{L}$ is the elastic stiffness tensor and $\mathbb{S}$ is the compliance tensor. Now, suppose we adopt the following Voigt notation, i.e,

$$\{\sigma\} = \begin{Bmatrix} \sigma_{11} \\ \sigma_{22} \\ \sigma_{12} \end{Bmatrix}, \ \{\varepsilon\} = \begin{Bmatrix} \varepsilon_{11} \\ \varepsilon_{22} \\ 2\varepsilon_{12} \end{Bmatrix}, \tag{30}$$

then both $\mathbb{L}$ and $\mathbb{S}$ can be represented by 3×3 matrices. Consider the following rotation in a 2D Cartesian coordinate system:

$$A = \begin{bmatrix} \cos\theta & \sin\theta \\ -\sin\theta & \cos\theta \end{bmatrix}, \tag{31}$$

which can be seen also as a coordinate transformation. The components of the strain tensor after such transformation are:

$$\varepsilon'_{ij} = A_{ik}A_{j\ell}\varepsilon_{k\ell}, \tag{32}$$

and in Voight notation, the above relation can be replaced by:

$$\{\varepsilon\}' = [N]\{\varepsilon\}, \tag{33}$$

with

$$[N] = \begin{bmatrix} A_{11}^2 & A_{12}^2 & A_{11}A_{12} \\ A_{21}^2 & A_{22}^2 & A_{21}A_{22} \\ 2A_{11}A_{21} & 2A_{12}A_{22} & A_{11}A_{22}+A_{12}A_{21} \end{bmatrix}, \tag{34}$$

and the transformation rule for the compliance matrix is:

$$[S]' = [N][S][N]^T. \tag{35}$$

Therefore, in principle, by rotating the coordinate system, the principal modulus/compliance direction can be determined. Due to symmetry, we only need to calculate half of the orientation range. Dividing this range into n equal parts, we calculate the material's Young's modulus in each rotated direction. The maximum value of calculated Young's modulus among these directions is the maximum Young's modulus, and its corresponding orientation is the orientation for the maximum Young's modulus.

Additional test on materials with circular-inclusions.

To examine the applicability of our framework beyond Gaussian Random Fields (GRFs), we conducted additional tests on materials with circular inclusion-type microstructures. These structures were generated by dividing the RVE into a 4×4 grid, as shown in Fig. S10 (a), within which each cell contains a randomly placed circular inclusion. The radius of each inclusion was sampled from a predefined probability distribution to induce variability in inclusion size and volume fraction.

Using our GNDM model, we observed that the learned latent variable c is able to capture the geometric characteristics related to inclusion fraction and correlated them with the effective modulus of the composite. Specifically, we found that as the inclusion area fraction increased, the effective modulus also increased, with a nonlinear proportional relationship reflected clearly in the learned latent space (Fig. S11 (c)). As shown in Fig. S11 (b), representative microstructures synthesized by sweeping a single latent coordinate c_1 from 0 to 1 . Increasing c_1 produces a smooth transition from sparse/small inclusions to dense/large arrays. These results confirm that our framework can generalize to microstructures beyond GRFs and remain effective in discovering interpretable, data-driven relationships between geometry and material properties.

Tables, figures

Table S1: Experimental results.

Figure. S1: A schematic diagram of the discriminator and the generator structures.

Figure. S2: Numerical data clusters for each pair of properties of three sets of parameters in three-parameter case.

Figure. S3: Tensile testing measurement definitions.

Figure. S4: Numerical simulation and target comparison.

Figure. S5: Effect of microstructure size on matching target properties.

Figure. S7- S7: Property distributions of the design parameters for three microstructure sizes (64×64,128×128,256×256) for selective parameters in experiment.

Figure. S8- S10: Functional gradient materials with Young's modulus, relative surface area and the orientations.

Figure. S11: Circular-inclusion microstructures illustration.

Table S1. Experimental results. Each data in the experimental results was obtained by testing three fabricated specimens for same samples. The upper and lower bounds of the reported experimental values were determined as the mean ± one standard deviation, calculated from the three measurements. Target denotes the material properties predicted using the phenomenological formula, *"Exp"* represents the properties obtained from experimental measurements, *"FEM"* corresponds to the properties computed via finite element simulations, and *"Num"* indicates the properties obtained through numerical calculations.

group	$\left(\frac{E}{E_{\text{hard}}}\right)_{\text{Target}}$	θ_{Target} (°)	RS_{Target}	$\left(\frac{E}{E_{\text{hard}}}\right)_{\text{Exp}}$	θ_{Exp} (°)	$\left(\frac{E}{E_{\text{hard}}}\right)_{\text{FEM}}$	θ_{FEM}	RS_{Num}
1	0.494	111.210	0.167	0.600 ± 0.020	125.303 ± 4.615	0.545	100.678	0.131
1	0.494	111.210	0.167	0.571 ± 0.152	105.417 ± 5.271	0.546	100.678	0.127
1	0.494	111.210	0.167	0.590 ± 0.109	113.244 ± 2.539	0.544	97.627	0.128
1	0.494	111.210	0.167	0.531 ± 0.057	116.999 ± 11.476	0.544	97.627	0.130
1	0.494	111.210	0.167	0.466 ± 0.049	120.292 ± 6.570	0.495	97.627	0.143
2	0.029	2.866	0.136	0.022 ± 0.000	18.505 ± 1.397	0.028	9.153	0.177
2	0.029	2.866	0.136	0.018 ± 0.001	18.720 ± 1.953	0.028	9.153	0.175
2	0.029	2.866	0.136	0.016 ± 0.000	24.074 ± 1.970	0.025	9.153	0.166
2	0.029	2.866	0.136	0.027 ± 0.004	15.244 ± 5.418	0.029	12.203	0.176
2	0.029	2.866	0.136	0.022 ± 0.002	19.575 ± 3.838	0.027	9.153	0.173
3	0.029	134.140	0.198	0.082 ± 0.007	131.695 ± 2.445	0.062	137.288	0.190
3	0.029	134.140	0.198	0.073 ± 0.006	133.277 ± 0.759	0.054	137.288	0.186
3	0.029	134.140	0.198	0.073 ± 0.010	132.079 ± 2.478	0.057	140.339	0.191
3	0.029	134.140	0.198	0.070 ± 0.010	121.483 ± 2.489	0.055	143.390	0.189
3	0.029	134.140	0.198	0.073 ± 0.001	129.025 ± 4.419	0.063	140.339	0.193
4	0.029	98.025	0.198	0.037 ± 0.000	118.707 ± 1.076	0.044	97.627	0.201
4	0.029	98.025	0.198	0.052 ± 0.002	115.720 ± 2.350	0.061	100.678	0.201
4	0.029	98.025	0.198	0.046 ± 0.002	112.040 ± 0.686	0.051	97.627	0.197
4	0.029	98.025	0.198	0.046 ± 0.002	106.917 ± 1.824	0.059	94.576	0.197
4	0.029	98.025	0.198	0.043 ± 0.002	111.835 ± 0.428	0.050	100.678	0.203
5	0.174	2.866	0.222	0.110 ± 0.017	18.590 ± 4.378	0.157	3.051	0.133
5	0.174	2.866	0.222	0.095 ± 0.009	5.767 ± 2.413	0.166	3.051	0.139
5	0.174	2.866	0.222	0.088 ± 0.009	5.604 ± 4.322	0.164	12.203	0.136
5	0.174	2.866	0.222	0.093 ± 0.007	20.966 ± 10.764	0.139	9.153	0.137
5	0.174	2.866	0.222	0.156 ± 0.007	6.714 ± 5.454	0.149	6.102	0.133
6	0.070	146.752	0.222	0.140 ± 0.008	154.019 ± 2.701	0.112	152.542	0.191
6	0.070	146.752	0.222	0.108 ± 0.003	153.894 ± 0.615	0.117	146.441	0.193
6	0.070	146.752	0.222	0.091 ± 0.005	160.545 ± 3.441	0.127	149.491	0.192
6	0.070	146.752	0.222	0.114 ± 0.005	149.629 ± 1.164	0.104	146.441	0.199
6	0.070	146.752	0.222	0.120 ± 0.007	150.781 ± 3.504	0.126	152.542	0.190
7	0.075	36.688	0.190	0.037 ± 0.004	32.122 ± 3.687	0.053	18.305	0.145
7	0.075	36.688	0.190	0.050 ± 0.003	39.407 ± 0.648	0.063	33.559	0.139
7	0.075	36.688	0.190	0.046 ± 0.004	41.008 ± 3.387	0.048	24.407	0.138
7	0.075	36.688	0.190	0.065 ± 0.002	38.723 ± 1.419	0.051	45.763	0.144
7	0.075	36.688	0.190	0.056 ± 0.004	41.417 ± 3.124	0.071	21.356	0.139
8	0.128	14.331	0.246	0.057 ± 0.004	18.199 ± 1.436	0.122	18.305	0.204
8	0.128	14.331	0.246	0.080 ± 0.007	23.741 ± 2.985	0.148	24.407	0.206
8	0.128	14.331	0.246	0.092 ± 0.005	19.193 ± 3.874	0.136	18.305	0.209
8	0.128	14.331	0.246	0.062 ± 0.005	19.616 ± 3.671	0.121	18.305	0.208
8	0.128	14.331	0.246	0.058 ± 0.002	22.897 ± 0.824	0.113	18.305	0.206
9	0.139	171.401	0.114	0.062 ± 0.007	165.532 ± 2.814	0.131	164.746	0.122
9	0.139	171.401	0.114	0.055 ± 0.004	174.028 ± 1.496	0.153	170.847	0.119
9	0.139	171.401	0.114	0.105 ± 0.011	158.918 ± 2.859	0.156	173.898	0.118
9	0.139	171.401	0.114	0.118 ± 0.015	151.360 ± 12.431	0.113	152.542	0.123

Continued on next page

Table S1. Experimental results. Each data in the experimental results was obtained by testing three fabricated specimens for same samples. The upper and lower bounds of the reported experimental values were determined as the mean ± one standard deviation, calculated from the three measurements. Target denotes the material properties predicted using the phenomenological formula, *"Exp"* represents the properties obtained from experimental measurements, *"FEM"* corresponds to the properties computed via finite element simulations, and *"Num"* indicates the properties obtained through numerical calculations.

group	$\left(\frac{E}{E_{\text{hard}}}\right)_{\text{Target}}$	θ_{Target} (°)	RS_{Target}	$\left(\frac{E}{E_{\text{hard}}}\right)_{\text{Exp}}$	θ_{Exp} (°)	$\left(\frac{E}{E_{\text{hard}}}\right)_{\text{FEM}}$	θ_{FEM}	RS_{Num}
9	0.139	171.401	0.114	0.101 ± 0.011	159.882 ± 2.969	0.127	176.949	0.122
10	0.436	145.605	0.089	0.360 ± 0.029	168.431 ± 0.910	0.456	152.542	0.093
10	0.436	145.605	0.089	0.445 ± 0.008	160.110 ± 2.249	0.419	155.593	0.099
10	0.436	145.605	0.089	0.347 ± 0.015	167.065 ± 1.868	0.426	155.593	0.098
10	0.436	145.605	0.089	0.411 ± 0.015	165.392 ± 5.219	0.392	152.542	0.098
10	0.436	145.605	0.089	0.493 ± 0.013	166.750 ± 3.319	0.411	152.542	0.101

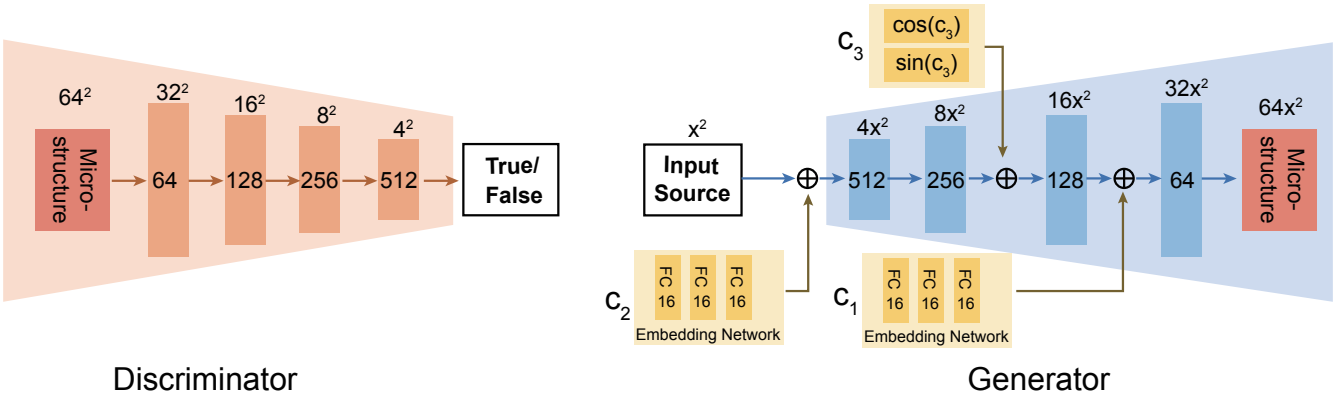

Figure S1. Network architecture of the discriminator and the generator. Discriminator (left): an input microstructure of size $64x^2$ is downsampled through $32x^2$, $16x^2$, $8x^2$, and $4x^2$ stages with $\{64, 128, 256, 512\}$ channels, followed by a binary real/fake head. Generator (right): an x^2 input source is upsampled through $4x^2/512 \rightarrow 8x^2/256 \rightarrow 16x^2/128 \rightarrow 32x^2/64$ to synthesize a $64x^2$ microstructure. Conditioning variables c_1 and c_2 pass through two-layer fully connected embedding networks (16 units each) and are concatenated ($\oplus$) with the corresponding feature maps; the angular parameter c_3 is encoded as $[\cos(c_3), \sin(c_3)]$ and injected at intermediate layers. Here, x denotes the base spatial resolution.

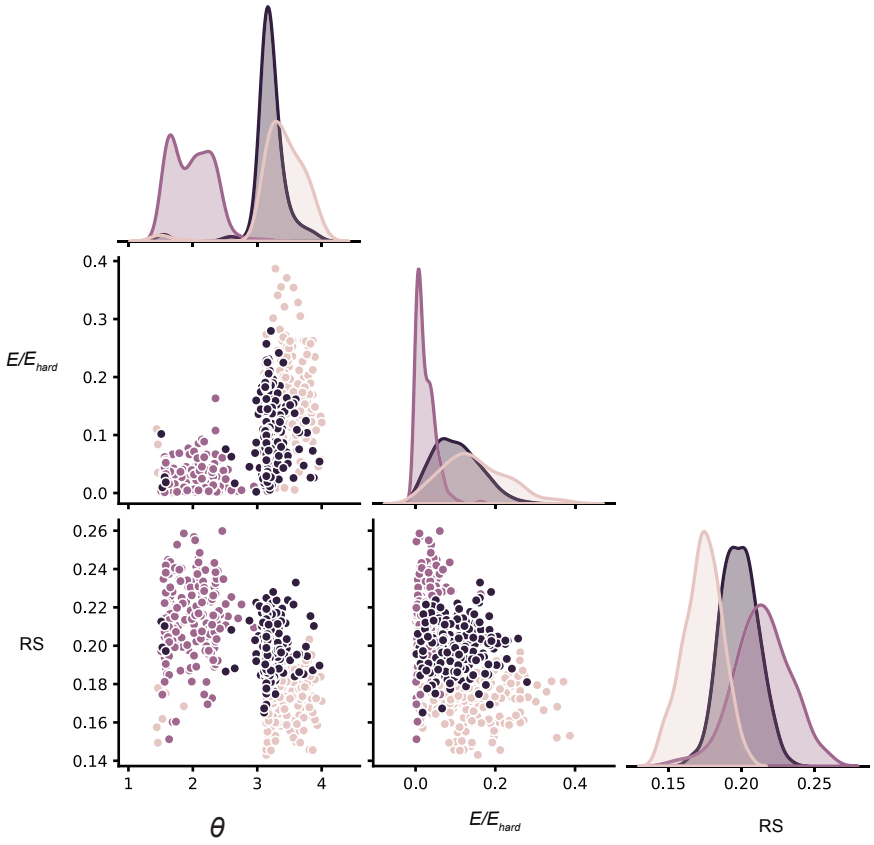

Figure S2. Property distributions of the generated samples. Numerical data clusters for each pair of properties of three sets of parameters in three-parameter case. Variables are θ, the normalized modulus E/E_{hard}, and RS. Colors denote three parameter sets, revealing distinct clusters and pairwise correlations between properties.

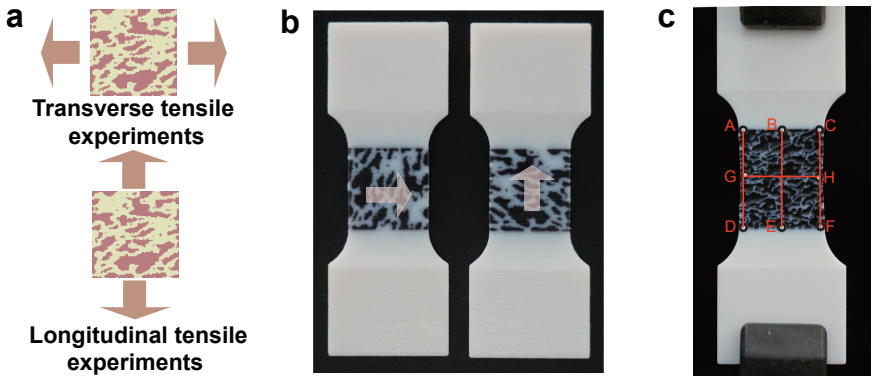

Figure S3. Tensile testing measurement setup. a, Each specimen was tested in two orthogonal uniaxial configurations: transverse and longitudinal tension of the microstructure samples. **b,** Photograph of the 3D-printed dog-bone samples; the dark central insert is the microstructure region. Arrows indicate the loading direction for the two tests. **c,** Points AH define the strain used to extract effective responses from the DIC displacement fields. Vertical gauges AD, BE, and CF provide axial strain, and the mid-height horizontal gauge GH gives transverse strain.

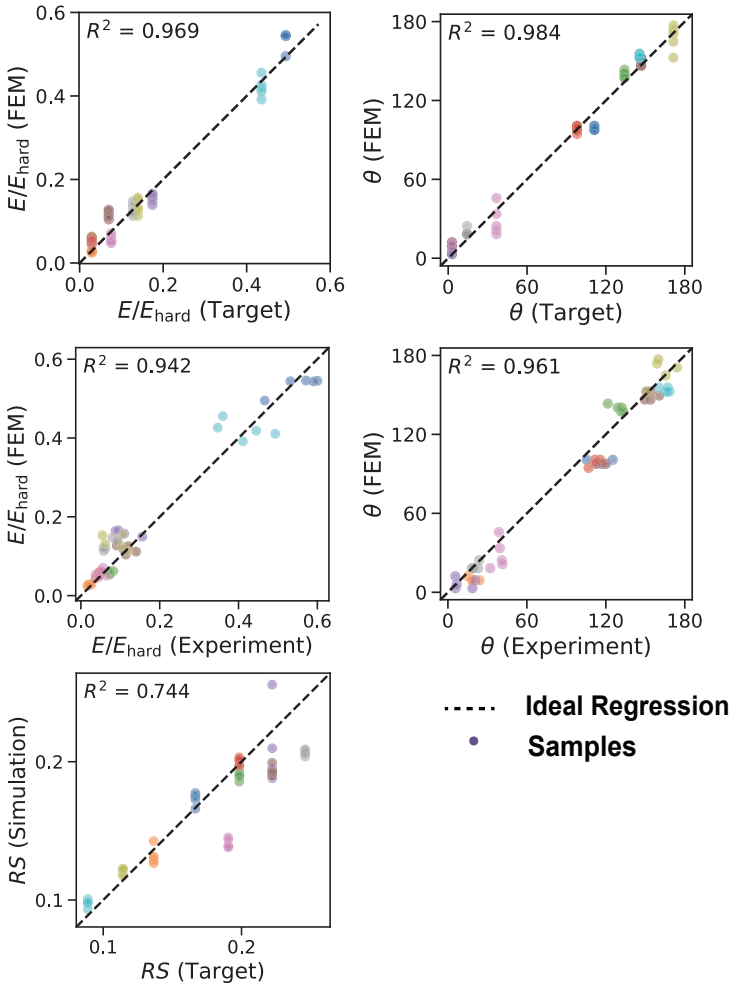

Figure S4. Comparison of target properties and FEM results.

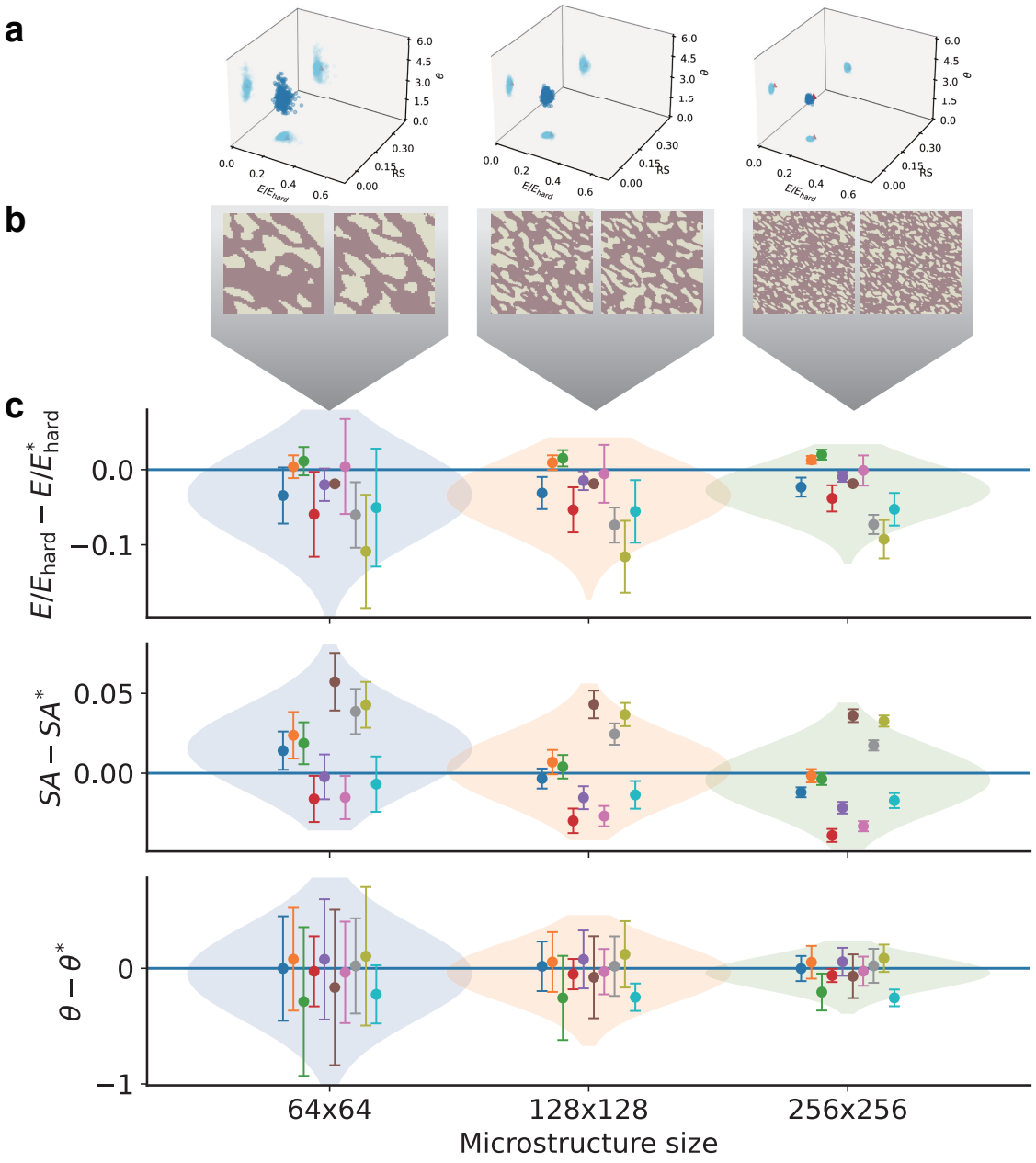

Figure S5. Effects of material sample sizes on the physical properties. a, Property distributions of the microstructural samples with different sizes: $64 \times 64, 128 \times 128, 256 \times 256$ pixels, generated by the same input geometric features. **b**, Below each cloud, two representative microstructures are shown. **c,** Comparison between experimental measurements and target properties for 10 random samples within each size group. The scatter points indicate deviations from the targets. The asterisks $(*)$ in the superscripts mark the target values.

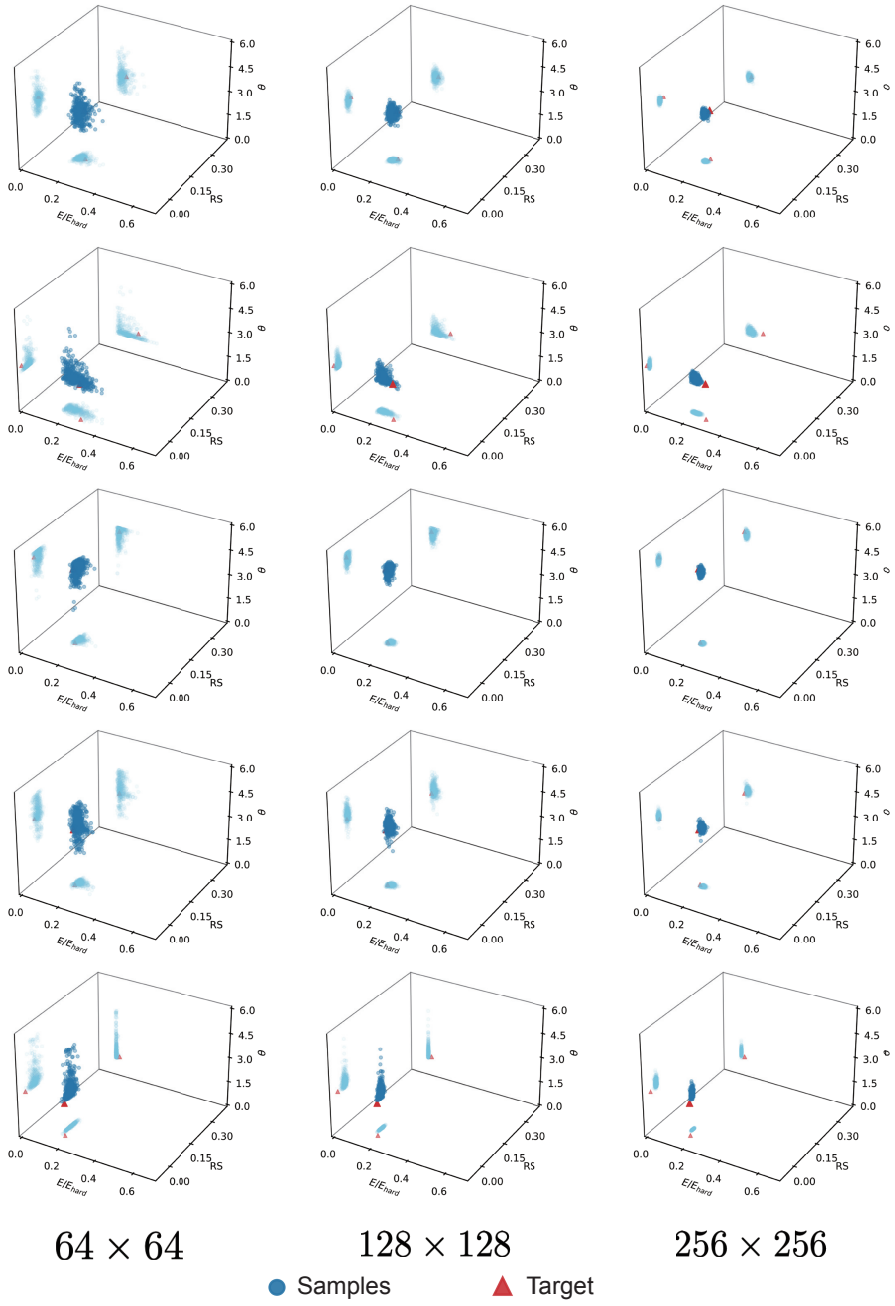

Figure S6. Property distributions of different groups of disordered material samples. Property distributions of the design parameters for three microstructure sizes (64×64,128×128,256×256) for the first five sets of parameters.

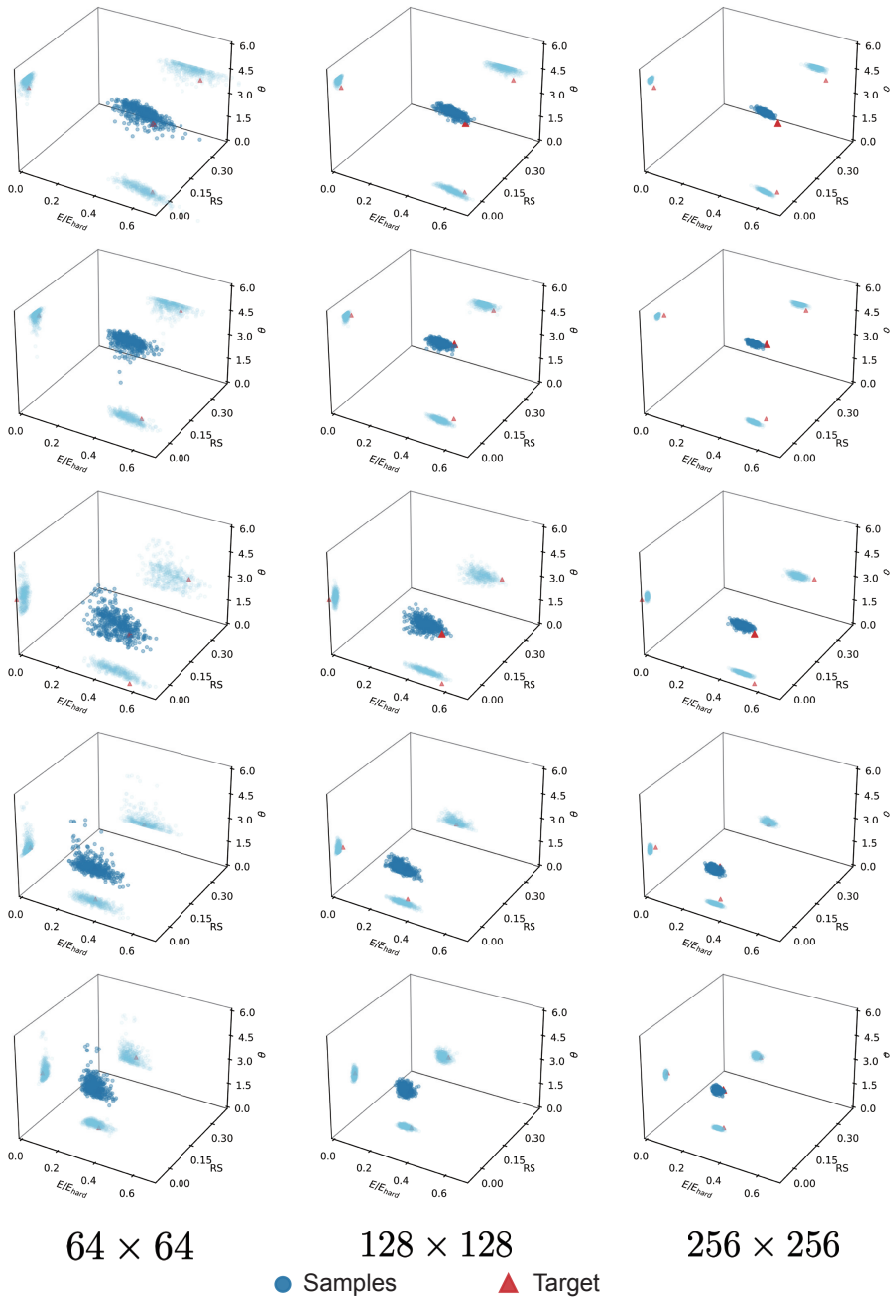

Figure S7. Property distributions of different groups of disordered material samples. Property distributions of the design parameters for three microstructure sizes (64×64,128×128,256×256) for the last five sets of parameters.

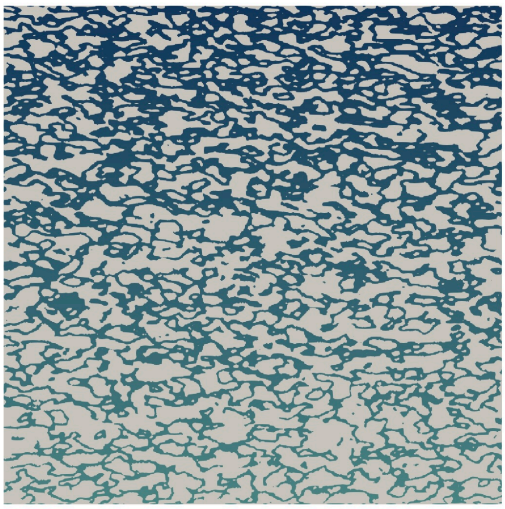

Figure S8. Functionally gradient materials with Young's modulus decreasing from top to bottom.

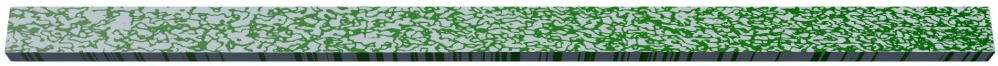

Figure S9. Functionally gradient materials with the relative surface area increasing from left to right.

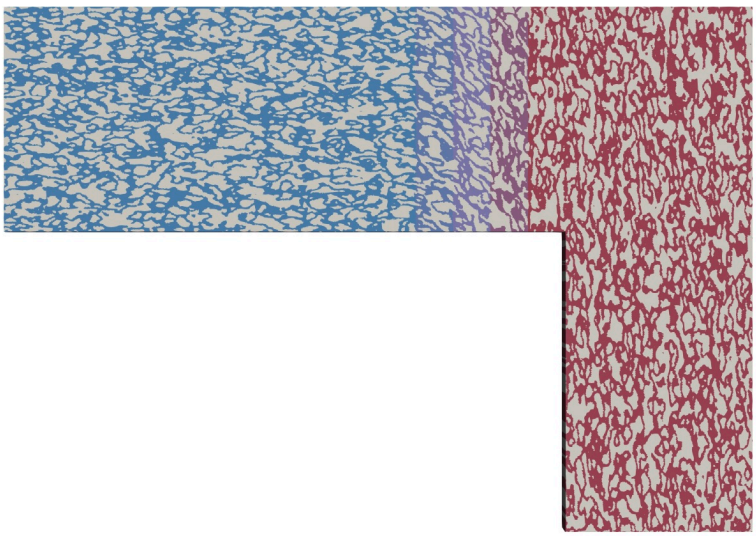

Figure S10. Functionally gradient materials with varying orientations of maximum Young's modulus.

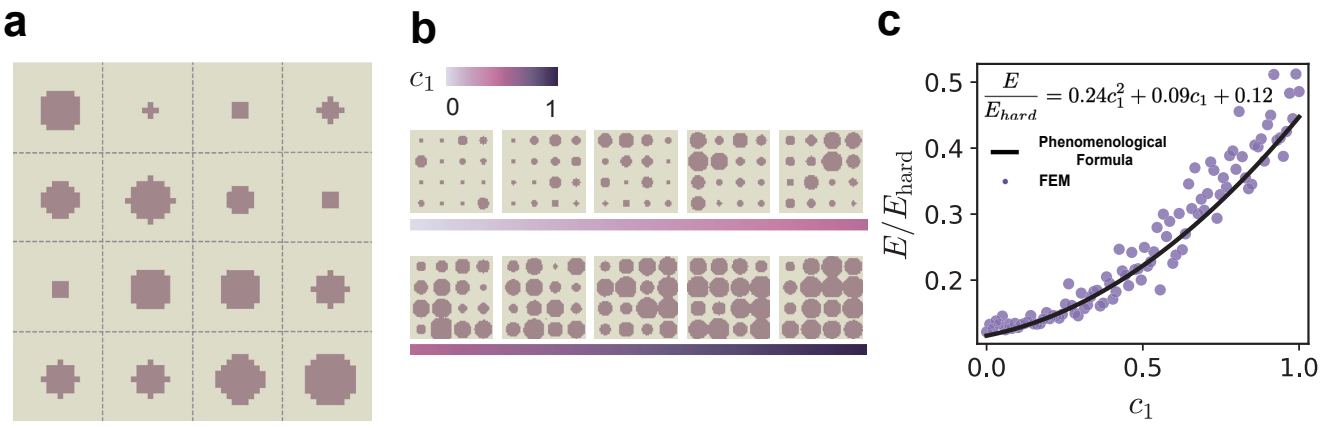

Figure S11. Additional validation of GNDM on materials with random circular-inclusions. a, Material microstructures of two-phase composites containing circular inclusions with random radii. **b,** Representative microstructures synthesized by sweeping a single latent dimension c_1 from 0 to 1 . Designs are ordered left-to-right; increasing c_1 produces a smooth transition from sparse/small inclusions to dense/large inclusions (color bar indicates the value of c_1). **c**, Effective in-plane stiffness normalized by the matrix modulus, E/E_{hard} , versus c_1, the solid curve shows the learned phenomenological formula.

Movie captions

Movie S1. AI-generated disordered microstructures with various target properties. By varying each dimension of the latent code **c** stepwise, the generated material microstructures transition gradually.

Movie S2. A composite cat with a heterogeneous distribution of material properties. The model generates structures with spatially varying local properties; applying loads at different locations induces distinct local deformation responses.

REFERENCES

1. L. J. Gibson, The hierarchical structure and mechanics of plant materials. *J. R. Soc. Interface* **9**, 2749–2766 (2012).

2. J. Aizenberg, J. C. Weaver, M. S. Thanawala, V. C. Sundar, D. E. Morse, P. Fratzl, Skeleton of Euplectellasp.: Structural hierarchy from the nanoscale to the macroscale. *Science* **309**, 275–278 (2005).

3. S. Krauss, E. Monsonego-Ornan, E. Zelzer, P. Fratzl, R. Shahar, Mechanical function of a complex three-dimensional suture joining the bony elements in the shell of the red-eared slider turtle. *Adv. Mater.* **21**, 407–412 (2009).

4. C. Perrin, Compositional heterogeneity and microstructural diversity of coral skeletons: Implications for taxonomy and control on early diagenesis. *Coral Reefs* **22**, 109–120 (2003).

5. A. Torres, A. A. Trikanad, C. A. Aubin, F. M. Lambers, M. Luna, C. M. Rimnac, P. Zavattieri, C. J. Hernandez, Bone-inspired microarchitectures achieve enhanced fatigue life. *Proc. Natl. Acad. Sci. U.S.A.* **116**, 24457–24462 (2019).

6. M. Zaiser, S. Zapperi, Disordered mechanical metamaterials *Nat. Rev.* **5**, 679–688 (2023).

7. H. Rhee, M. Horstemeyer, Y. Hwang, H.-S. Lim, H. Kadiri, W. Trim, A study on the structure and mechanical behavior of the *terrapene carolina* carapace: A pathway to design bio-inspired synthetic composites. *Mater. Sci. Eng. C* **29**, 2333–2339 (2009).

8. J. T. Overvelde, K. Bertoldi, Relating pore shape to the non-linear response of periodic elastomeric structures. *J. Mech. Phys. Solids* **64**, 351–366 (2014).

9. C. M. Portela, A. Vidyasagar, S. Krödel, T. Weissenbach, D. W. Yee, J. R. Greer, D. M. Kochmann, Extreme mechanical resilience of self-assembled nanolabyrinthine materials. *Proc. Natl. Acad. Sci. U.S.A.* **117**, 5686–5693 (2020).

10. P. Wang, F. Yang, B. Zheng, P. Li, R. Wang, Y. Li, H. Fan, X. Li, Breaking the tradeoffs between different mechanical properties in bioinspired hierarchical lattice metamaterials. *Adv. Funct. Mater.* **33**, 2305978 (2023).

11. F. Wang, M. Brøns, O. Sigmund, Non-hierarchical architected materials with extreme stiffness and strength. *Adv. Funct. Mater.* **33**, 2211561 (2023).

12. D. Schurig, J. J. Mock, B. J. Justice, S. A. Cummer, J. B. Pendry, A. F. Starr, D. R. Smith, Metamaterial electromagnetic cloak at microwave frequencies. *Science* **314**, 977–980 (2006).

13. F. Magnus, B. Wood, J. Moore, K. Morrison, G. Perkins, J. Fyson, M. C. K. Wiltshire, D. Caplin, L. F. Cohen, J. B. Pendry, A d.c. magnetic metamaterial. *Nat. Mater.* **7**, 295–297 (2008).

14. J. Li, L. Fok, X. Yin, G. Bartal, X. Zhang, Experimental demonstration of an acoustic magnifying hyperlens. *Nat. Mater.* **8**, 931–934 (2009).

15. N. Fang, D. Xi, J. Xu, M. Ambati, W. Srituravanich, C. Sun, X. Zhang, Ultrasonic metamaterials with negative modulus. *Nat. Mater.* **5**, 452–456 (2006).

16. T. A. Schaedler, A. J. Jacobsen, A. Torrents, A. E. Sorensen, J. Lian, J. R. Greer, L. Valdevit, W. B. Carter, Ultralight metallic microlattices. *Science* **334**, 962–965 (2011).

17. J. I. Lipton, R. MacCurdy, Z. Manchester, L. Chin, D. Cellucci, D. Rus, Handedness in shearing auxetics creates rigid and compliant structures. *Science* **360**, 632–635 (2018).

18. C. Luo, Y. Song, C. Zhao, S. Thirumalai, I. Ladner, M. A. Cullinan, J. B. Hopkins, Design and fabrication of a three-dimensional meso-sized robotic metamaterial with actively controlled properties. *Mater. Horiz.* **7**, 229–235 (2020).

19. M. J. Silva, L. J. Gibson, The effects of non-periodic microstructure and defects on the compressive strength of two-dimensional cellular solids. *Int. J. Mech. Sci.* **39**, 549–563 (1997).

20. R. A. Metzler, F. Barthelat, J. J. Wilker, Disordered structures in biology can provide material properties not obtained with precise hierarchy. *Adv. Funct. Mater.* **29**, 1805734 (2019).

21. D. Rayneau-Kirkhope, S. Bonfanti, S. Zapperi, Density scaling in the mechanics of a disordered mechanical meta-material. *Appl. Phys. Lett.* **114**, 111902 (2019).

22. Y. Jia, K. Liu, X. S. Zhang, Modulate stress distribution with bio-inspired irregular architected materials towards optimal tissue support. *Nat. Commun.* **15**, 4072 (2024).

23. D. R. Reid, N. Pashine, J. M. Wozniak, H. M. Jaeger, A. J. Liu, S. R. Nagel, J. J. de Pablo, Auxetic metamaterials from disordered networks. *Proc. Natl. Acad. Sci. U.S.A.* **115**, E1384–E1390 (2018).

24. Y. Liu, B. Xia, K. Liu, Y. Zhou, K. Wei, Robustness and diversity of disordered structures on sound absorption and deformation resistance. *J. Mech. Phys. Solids* **190**, 105751 (2024).

25. K. Liu, R. Sun, C. Daraio, Growth rules for irregular architected materials with programmable properties. *Science* **377**, 975–981 (2022).

26. M. A. Bessa, R. Bostanabad, Z. Liu, A. Hu, D. W. Apley, C. Brinson, W. Chen, W. K. Liu, A framework for data-driven analysis of materials under uncertainty: Countering the curse of dimensionality. *Comput. Method Appl. Mech. Eng.* **320**, 633–667 (2017).

27. S. Torquato, H. Haslach Jr, Random heterogeneous materials: Microstructure and macroscopic properties. *Appl. Mech. Rev.* **55**, B62–B63 (2002).

28. A. J. Lew, K. Jin, M. J. Buehler, Designing architected materials for mechanical compression via simulation, deep learning, and experimentation. *NPJ Comput. Mater.* **9**, 80 (2023).

29. D. Lee, W. (W.) Chen, L. Wang, Y.C. Chan, W. Chen, Data-driven design for metamaterials and multiscale systems: A review. *Adv. Mater.* **36**, e2305254 (2024).

30. R. Kulagin, Y. Beygelzimer, Y. Estrin, A. Schumilin, P. Gumbsch, Architectured lattice materials with tunable anisotropy: Design and analysis of the material property space with the aid of machine learning. *Adv. Eng. Mater.* **22**, 2001069 (2020).

31. R. Van Mastrigt, M. Dijkstra, M. van Hecke, C. Coulais, Machine learning of implicit combinatorial rules in mechanical metamaterials. *Phys. Rev. Lett.* **129**, 198003 (2022).

32. B. Peng, Y. Wei, Y. Qin, J. Dai, Y. Li, A. Liu, Y. Tian, L. Han, Y. Zheng, P. Wen, Machine learning-enabled constrained multi-objective design of architected materials. *Nat. Commun.* **14**, 6630 (2023).

33. Z. Yu, P. Thakolkaran, K. Shea, T. Stanković, Artificial neural network supported design of a lattice-based artificial spinal disc for restoring patient-specific anisotropic behaviors. *Comput. Biol. Med.* **152**, 106475 (2023).

34. S. Kumar, S. Tan, L. Zheng, D. M. Kochmann, Inverse-designed spinodoid metamaterials. *NPJ Comput. Mater.* **6**, 73 (2020).

35. F. V. Senhora, E. D. Sanders, G. H. Paulino,Optimally-tailored spinodal architected materials for multiscale design and manufacturing. *Adv. Mater.* **34**, e2109304 (2022).

36. B. Li, C. Huang, X. Li, S. Zheng, J. Hong, Non-iterative structural topology optimization using deep learning. *Comput. Aided Des.* **115**, 172–180 (2019).

37. A. H. Nobari, W. Chen, F. Ahmed, Range-constrained generative adversarial network: Design synthesis under constraints using conditional generative adversarial networks. *J. Mech. Des.* **144**, 021708 (2022).

38. S. Noguchi, J. Inoue, Stochastic characterization and reconstruction of material microstructures for establishment of process-structure-property linkage using the deep generative model. *Phys. Rev. E* **104**, 025302 (2021).

39. I. Goodfellow, J. Pouget-Abadie, M. Mirza, B. Xu, D. Warde-Farley, S. Ozair, A. Courville, Y. Bengio, Generative adversarial networks. *Commun. ACM* **63**, 139–144 (2020).

40. I. Gulrajani, F. Ahmed, M. Arjovsky, V. Dumoulin, A. Courville, Improved training of wasserstein gans. *Adv. Neural Inf. Process Syst.* **30**, 5769–5779 (2017).

41. X. Chen, A. Karbasi, F.W. Crawford, Estimating the size of a large network and its communities from a random sample. *Adv. Neural Inf. Process Syst.* **29**, 3072–3080 (2016).

42. B. Zhu, M. Skouras, D. Chen, W. Matusik, Two-scale topology optimization with microstructures. *ACM Trans. Graph.* **36**, 1 (2017).

43. L. Makatura, B. Wang, Y.L. Chen, B. Deng, C. Wojtan, B. Bickel, W. Matusik, Procedural metamaterials: A unified procedural graph for metamaterial design. *ACM Trans. Graph.* **42**, 1–19 (2023).

44. H. Li, Z. Luo, L. Gao, Q. Qin, Topology optimization for concurrent design of structures with multi-patch microstructures by level sets. *Comput. Methods Appl. Mech. Eng.* **331**, 536–561 (2018).

45. M. Xiao, X. Liu, Y. Zhang, L. Gao, J. Gao, S. Chu, Design of graded lattice sandwich structures by multiscale topology optimization. *Comput. Methods Appl. Mech. Eng.* **384**, 113949 (2021).

46. G. Bertolino, M. Montemurro, Two-scale topology optimisation of cellular materials under mixed boundary conditions. *Int. J. Mech. Sci.* **216**, 106961 (2022).

47. F. Liu, Z. Mao, P. Zhang, D. Z. Zhang, J. Jiang, Z. Ma, Functionally graded porous scaffolds in multiple patterns: New design method, physical and mechanical properties. *Mater. Des.* **160**, 849–860 (2018).

48. M. F. Ashby, L. J. Gibson, Cellular solids: Structure and properties (Cambridge Univ. Press, 1997), pp. 175–231.

49. K. Sano, Y. Ishida, T. Aida, Synthesis of anisotropic hydrogels and their applications. *Angew. Chem. Int. Ed.* **57**, 2532–2543 (2018).

50. A. Radford, L. Metz, S. Chintala, Unsupervised representation learning with deep convolutional generative adversarial networks. arXiv:1511.06434 [cs.LG] (2015).

51. T. Salimans, W. Zaremba, V. Cheung, X. Chen, I. Goodfellow, A. Radford, Improved techniques for training gans. *Adv. Neural Inf. Process. Syst.* **29**, 6597–6607 (2016).

52. H. De Vries, F. Strub, J. Mary, H. Larochelle, O. Pietquin, A. Courville, Modulating early visual processing by language. *Adv. Neural Inf. Process. Syst.* **30**, (2017).

53. G. Bradski, The opencv library. *Dr. Dobb's Journal: Software Tools for the Professional Programmer* **25**, 120–123 (2000).

54. J. Fish, *Practical Multiscaling* (John Wiley & Sons, 2013).